HHS Public Access

Author manuscript

Nanoscale. Author manuscript; available in PMC 2015 July 29.

Published in final edited form as:

Nanoscale. 2014 May 21; 6(10): 5284–5288. doi:10.1039/c4nr00497c.

Europium- and lithium-doped yttrium oxide nanocrystals that provide a linear emissive response with X-ray radiation exposure†

Ian N. Stanton[a], **Matthew D. Belley**[b], **Giao Nguyen**[c], **Anna Rodrigues**[b], **Yifan Li**[d], **David G. Kirsch**[d,e], **Terry T. Yoshizumi**[c,d], and **Michael J. Therien**[a]

Michael J. Therien: michael.therien@duke.edu

[a]Department of Chemistry, French Family Science Center, Duke University, 124 Science Drive, Durham, North Carolina 27708, USA. Fax: +1 919 684 1522, Tel: +1 919 660 1670

[b]Medical Physics Graduate Program, Duke University, Hock Plaza, 2424 Erwin Road, Durham, NC 27705, USA

[c]Department of Radiology, Duke University Medical Center, 2214 Elder Street, Durham, NC 27710, USA

[d]Department of Radiation Oncology, Duke University Medical Center, Box 91006, Durham, NC 27708, USA

[e]Department of Pharmacology and Cancer Biology, Duke University School of Medicine, Box 3813, Durham, NC 27710, USA

Abstract

Eu- and Li-doped yttrium oxide nanocrystals [$Y_{2-x}O_3$; Eu_x, Li_y], in which Eu and Li dopant ion concentrations were systematically varied, were developed and characterized (TEM, XRD, Raman spectroscopic, UV-excited lifetime, and ICP-AES data) in order to define the most emissive compositions under specific X-ray excitation conditions. These optimized [$Y_{2-x}O_3$; Eu_x, Li_y] compositions display scintillation responses that: (i) correlate linearly with incident radiation exposure at X-ray energies spanning from 40–220 kVp, and (ii) manifest no evidence of scintillation intensity saturation at the highest evaluated radiation exposures [up to 4 Roentgen per second]. For the most emissive nanoscale scintillator composition, [$Y_{1.9}O_3$; $Eu_{0.1}$, $Li_{0.16}$], excitation energies of 40, 120, and 220 kVp were chosen to probe the dependence of the integrated emission intensity upon X-ray exposure-rate in energy regimes having different mass-attenuation coefficients and where either the photoelectric or the Compton effect governs the scintillation mechanism. These experiments demonstrate for the first time for that for comparable radiation exposures, when the scintillation mechanism is governed by the photoelectric effect and a comparably larger mass-attenuation coefficient (120 kVp excitation), greater integrated emission intensities are recorded relative to excitation energies where the Compton effect regulates scintillation (220 kVp) in nanoscale [$Y_{2-x}O_3$; Eu_x] crystals. Nanoscale [$Y_{1.9}O_3$; $Eu_{0.1}$, $Li_{0.16}$] (70

†Electronic supplementary information (ESI) available: Material synthesis; experimental details; X-ray diffraction (XRD), UV-excited lifetimes, ICP-AES, and additional TEM data.

Correspondence to: Michael J. Therien, michael.therien@duke.edu.

± 20 nm) was further exploited as a detector material in a prototype fiber-optic radiation sensor. The scintillation intensity from the [$Y_{1.9}O_3$; $Eu_{0.1}$, $Li_{0.16}$]-modified, 400 μm sized optical fiber tip, recorded using a CCD-photodetector and integrated over the 605–617 nm wavelength domain, was correlated with radiation exposure using a Precision XRAD 225Cx small-animal image guided radiation therapy (IGRT) system. For both 80 and 225 kVp energies, this radio transparent device recorded scintillation intensities that tracked linearly with total radiation exposure, highlighting its capability to provide alternately accurate dosimetry measurements for both diagnostic imaging (80 kVp) and radiation therapy treatment (225 kVp).

Introduction

Inorganic scintillators have long been exploited as radiation sensing materials due to their high stabilities and emission characteristics, and the fact that the emissive wavelengths of these species are compatible with conventional photomultiplier tubes.[1–3] Factors such as crystal growth conditions and the need for cryogenic cooling, for example, have limited the extent to which many of these materials can be deployed. Modern photodetectors, such as those based on CCD cameras and Si-photodiodes, enable enhanced scintillation emission detection sensitivities, and open up new possibilities to exploit scintillators that are smaller, easier to produce, and scintillate within the photodetector spectral regime that affords optimal quantum efficiency of the photovoltaic response (generally between 500 and 1000 nm).

Bulk yttrium oxide activated with europium ions, [Y_2O_3; Eu], has been utilized as the red-phosphor in early cathode ray televisions[4] and as the scintillator material in a wide variety of X-ray computed tomography (CT) detectors:[5] both of these applications exploit the material's peak emissions near 600 nm. While nanoscale [Y_2O_3; Eu] has found utility in white light emitting diodes[6] and *in vitro* imaging,[7] its X-ray scintillation properties have yet to be fully interrogated, despite the fact that the per-mass scintillation yield of highly crystalline [Y_2O_3; Eu] nanoscale materials was shown to exceed that of their bulk counterparts under electron-beam excitation.[8] Further, while scintillating nanomaterials have been delineated and demonstrate considerable potential,[9–13] relatively little work has capitalized upon such materials in device architectures.

In this report, we describe Eu- and Li-doped yttrium oxide nanocrystals [$Y_{2-x}O_3$; Eu_x, Li_y] in which dopant ion concentrations have been systematically varied in order to define the most emissive compositions under specific sets of X-ray excitation conditions. We show that [$Y_{2-x}O_3$; Eu_x, Li_y] compositions display scintillation responses that: (i) correlate linearly with incident radiation exposure at X-ray energies spanning from 40–220 kVp, and (ii) manifest no evidence of scintillation intensity saturation at the highest evaluated radiation exposures [up to 4 Roentgen per second (R s^{-1}; 1 $R = 2.58 \times 10^{-4}$ Coulombs of charge produced by X- or γ-rays per kilogram of air)]. We further show that the most emissive of these nanoscale scintillator compositions provides a linear emission response as a function of radiation exposure for 80 and 225 kVp X-ray energies in a micro-CT dual imaging and high precision cone-beam therapy instrument utilized for small-animal image guided radiation therapy (IGRT).

Results and discussion

The flame-combustion technique, utilizing glycine and metal nitrate salts at a fixed ratio, was employed to systematically synthesize nanocrystal compositions.[14,15] X-ray diffraction (XRD) spectra confirmed that all compositions displayed a cubic structure, and inductively coupled plasma atomic emission spectroscopy (ICP-AES) provided [$Y_{2-x}O_3$; Eu_x, Li_y] compositional analysis (Fig. S1; Table S1, ESI†). Fig. 1A and B display representative TEM images of the most emissive Eu-doped [$Y_{1.9}O_3$; $Eu_{0.1}$] and Eu/Li co-doped [$Y_{1.9}O_3$; $Eu_{0.1}$, $Li_{0.16}$] compositions determined for 130 kVp (5 mA) X-ray excitation. Analyses of the Fig. 1 TEM images, and the TEM images for the [$Y_{1.9}O_3$; $Eu_{0.1}$, Li_y] compositional series (y = 0 to 0.25; Fig. S2†), reveal that as Li doping is increased from y = 0 to y = 0.25, crystalline size increases from ∼20–40 nm to ∼50–90 nm, and crystalline boundaries become better defined. Increased nanocrystal sizes and the corresponding reduction of amorphous content are evident in TEM images and the Raman spectra of these samples; note that as the Li ion doping concentration increases, the Raman scattering intensity of the dominant optical phonon of cubic-Y_2O_3 at 376 cm^{-1} increases (Fig. 1C), congruent with data acquired for corresponding heterogeneous bulk-phase samples.[16] While increased levels of Li ion doping of bulk phase [Y_2O_3; Eu] compositions have been demonstrated to track qualitatively with augmented cathodoluminescence intensity,[17, 18] the experimental data presented herein highlight that the increased nanoscale size and crystallinity of the Y_2O_3 host lattice that occurs with Li^+ doping also results in an increased scintillation intensity of the nanocrystalline [$Y_{2-x}O_3$; Eu_x, Li_y] compositions (*vide infra*).

To obtain [$Y_{2-x}O_3$; Eu_x, Li_y] compositions that display enhanced emission, Eu concentrations were initially varied over a [$Y_{1.98}O_3$; $Eu_{0.02}$] to [$Y_{1.69}O_3$; $Eu_{0.31}$] compositional range, and interrogated *via* solid-state X-ray emission spectroscopy (XES) using a 130 kVp (5 mA) X-ray cabinet-confined irradiation source. In these studies, 5 mg of [$Y_{2-x}O_3$; Eu_x] nanocrystals were pressed into a 7 mm diameter disk and placed on a Teflon mount; an optical fiber was utilized to collect scintillated emission, which was quantitated using an Edinburgh FLS920 spectrometer (ESI†). These studies demonstrated that the [$Y_{1.9}O_3$; $Eu_{0.1}$] composition was the most emissive member of this compositional series; Fig. 2A displays the X-ray emission intensities determined over a 575–675 nm range for these nanoscale [Y_2O_3; Eu_x] compositions. Note that this experimental trend in X-ray emission intensity determined as a function of Eu ion concentration depicts characteristic activator ion emission behavior in yttrium oxide host crystals,[4, 19–21] *i.e.*, an optimal concentration of emitting ions exists, beyond which cross-ion quenching drives reductions of X-ray emission intensity.

Holding the optimized Eu activator ion concentration of [$Y_{1.9}O_3$; $Eu_{0.1}$] constant, progressively increasing Li ion concentrations were incorporated into combustion reactions used to synthesize the [$Y_{1.9}O_3$; $Eu_{0.1}$, Li_y] compositions; ICS-AES was used to determine the ion doping levels of the isolated nanocrystalline products (Table S1†). Fig. 2B shows the integrated solid-state X-ray emission intensities determined over a 575–675 nm range for [$Y_{1.9}O_3$; $Eu_{0.1}$, Li_y] (y = 0 to 0.25) compositions recorded for 130 kVp (5 mA) X-ray excitation. These XES data show that [$Y_{1.9}O_3$; Eu_{01}, $Li_{0.16}$] is the most emissive of the [$Y_{1.9}O_3$; $Eu_{0.1}$, Li_y] compositions under these conditions, displaying more than twice the

emission intensity of the parent [$Y_{1.9}O_3$; $Eu_{0.1}$] nanocrystalline material (Fig. 2C). Emission lifetime data acquired for these [$Y_{1.9}O_3$; $Eu_{0.1}$, Li_y] (y = 0 to 0.25) compositions utilizing pulsed-lamp UV-excitation of the Eu–O charge transfer band showed that each composition displayed a single exponential lifetime decay of 2.12 ± 0.04 ms (Fig. S3†). These identical emissive lifetimes, along with TEM and Raman spectroscopic data (Fig. 1), indicate that the emission intensity augmentation observed under X-ray excitation with Li-doping results from the enhanced quantum efficiency of the larger, more crystalline nanocrystals on a per-unit mass basis; earlier literature notes that this effect derives from a combination of reduced surface quenching sites, increased phonon-electron coupling, and diminished internal reflections in more crystalline samples.[17,22–24]

Energy and flux dependent X-ray emission spectroscopic measurements of the most emissive nanoscale composition, [$Y_{1.9}O_3$; $Eu_{0.1}$, $Li_{0.16}$], were determined for solid-state samples at 40,120, and 220 kVp excitation through modulation of the X-ray tube current (mA). For a given X-ray tube voltage, the tube current was adjusted in 2–5 mA steps to provide a range of X-ray exposure rates (R s^{-1}). Fig. 3 shows the linear response of the integrated emission intensity over the 500–700 nm emission range recorded for 40, 120, and 220 kVp X-ray excitation energies. For 120 and 220 kVp excitation, integrated scintillation intensities were recorded over identical exposure-rate ranges (0.6–4.0 R s^{-1}) in order to assess the energy dependence of the scintillation intensity. Note that the dependences of scintillation intensity upon radiation dose differ slightly at these two excitation energies (Fig. 3B and C), as the slope determined at 120 kVp surpasses that at 220 kVp by a factor of 1.2. As both of these X-ray excitation energies exceed that of the yttrium k-edge (17 keV), this effect is congruent with the facts that (i) yttriumoxide displays a higher mass-attenuation coefficient (ionizing radiation absorption) at 120 kVp than 220 kVp,[25] and (ii) the scintillation mechanism is dominated by the photoelectric effect at 120 kVp, and the Compton effect at 220 kVp, for yttrium's Z-number of 39.[26] These data further underscore that the scintillation intensity observed for the nanoscale [$Y_{1.9}O_3$; $Eu_{0.1}$, $Li_{0.16}$] composition for photoelectric energy region absorption exceeds that for Compton energy region absorption, for comparable high-energy photon exposures and this nanocrystalline lattice.

The spectroscopically demonstrated linear response of scintillation intensity with X-ray energy and flux for these nanocrystals, across broad, medically relevant energy and exposure ranges (Fig. 3), underscores the potential utility of these nanomaterials. As such, a prototype device for measuring radiation exposure (dosimetry), based on the most emissive nanoscale composition, was developed. [$Y_{1.9}O_3$; Eu_{01}, $Li_{0.16}$] nanocrystals (1 mg) were pressed into a 7 mm flat disk; a fractured piece of ∼400 um diameter (∼3.3 μg) was employed as the device detection element, and optically-glued to one end of a 400 μm (inner diameter) optical fiber. The other end of the fiber was connected to a high-sensitivity, high-spectral resolution CCD-spectrometer (Fig. 4A). The scintillation intensity from the [$Y_{1.9}O_3$; $Eu_{0.1}$, $Li_{0.16}$]-modified optical fiber tip, integrated over the 605–617 nm wavelength domain (note that this integration range is limited by the CCD-spectrometer spectral window), was correlated with radiation exposure using a Precision XRAD 225Cx small-animal image guided radiation therapy (IGRT) system, in order to highlight the relevance of this prototype device to *in vivo* radiation dosimetry. A key feature of the

Precision XRAD 225Cx instrument is that it employs low dose X-ray computed tomography (CT) to image a specific organ or tissue area of interest, prior to delivery of therapeutic X-ray doses *via* an X-ray pencil-beam that targets millimeter-sized areas of malignant tissue at high precision, thus minimizing healthy tissue damage.[27] The spatial dimensions of the X-ray pencil-beam precludes use of conventional dosimetry devices to measure the radiation dose delivered to small treatment areas, and thus underscore one potential role for nanoscale scintillating materials in medicine.

Fig. 4B shows an X-ray image taken at 40 kVp of the fiberoptic device next to a standard ion-chamber radiation detector used to calibrate the radiation exposure on the Precision XRAD 225Cx image guided radiation therapy (IGRT) system. Note that the copper wires present in the ion-chamber show dark contrast, highlighting that the sensor portion of the prototype detector based on nanoscale [$Y_{1.9}O_3$; $Eu_{0.1}$, $Li_{0.16}$] is effectively radiotransparent during diagnostic imaging, due to the low-density, low Z-number, and small size of the fiber-optic. The radio transparency of the fiber-optic device underscores its *in vivo* utility with the IGRT system as it alternately provides accurate dosimetry measurements for both diagnostic imaging and radiation therapy treatment, while precluding the possibility for significant imaging artefacts that accompany the use of ion chamber- or MOSFET-based dosimeters.

Fig. 4C displays a plot of integrated scintillation intensity (605–617 nm) *versus* total radiation exposure at both 80 kVp (diagnostic imaging) and 225 kVp (therapy) energies. As noted earlier for data that compared emission intensity for 120 and 220 kVp excitations at equivalent exposures (Fig. 3B and C) for the [$Y_{1.9}O_3$; $Eu_{0.1}$, $Li_{0.16}$] composition, 80 kVp incident x-rays produce more light than do 225 kVp x-rays over identical 0–6 Roentgen exposure ranges, further highlighting this nano-material is more emissive when the scintillation mechanism is dominated by the photoelectric effect. Since the entire scintillation spectrum, not just a single scintillation wavelength, expresses a linear response with respect to radiation exposure (Fig. 3A-C), simple device architectures that exploit Si-photo-diodes can be fabricated that take advantage of the fact that the Si photodiode offers maximal sensitivity over the emission range of nanoscale [$Y_{1.9}O_3$; Eu_{01}, $Li_{0.16}$]. Note that such devices that exploit rare-earth doped inorganic nanocrystals will compliment pioneering optical fiber dosimeters that are based on plastic scintillating materials,[28–30] while providing superior environmental and radiation stability, new scintillation energy ranges, and the opportunity for significantly red-shifted luminescence, in a device architecture that provides fast timing speeds, small size, and low power-consumption.

Conclusions

In summary, Eu- and Li-doped yttrium oxide nanocrystals [$Y_{2-x}O_3$; Eu_x, Li_y] in which Eu and Li dopant ion concentrations were systematically varied, were developed and characterized (TEM, XRD, Raman spectroscopic, UV-excited lifetime, and ICP-AES data) in order to define the most emissive compositions under specific X-ray excitation conditions. These optimized [$Y_{2-x}O_3$; Eu_x, Li_y] compositions display scintillation responses that: (i) correlate linearly with incident radiation exposure at X-ray energies spanning from 40–220 kVp, and (ii) manifest no evidence of scintillation intensity saturation at the highest

evaluated radiation exposures [up to 4 Roentgen per second]. For the most emissive nanoscale scintillator composition, [$Y_{1.9}O_3$; $Eu_{0.1}$, $Li_{0.16}$], excitation energies of 40, 120, and 220 kVp were chosen to probe the dependence of the integrated emission intensity upon X-ray exposure-rate in energy regimes having different mass-attenuation coefficients and where either the photoelectric or the Compton effect governs the scintillation mechanism. These experiments demonstrate for the first time for that for comparable radiation exposures, when the scintillation mechanism is governed by the photoelectric effect and a comparably larger mass-attenuation coefficient (120 kVp excitation), greater integrated emission intensities are recorded relative to excitation energies where the Compton effect regulates scintillation (220 kVp) in nanoscale [$Y_{2-x}O_3$; Eu_x] crystals. Nanoscale [$Y_{1.9}O_3$; $Eu_{0.1}$, $Li_{0.16}$] (70 ± 20 nm) was further exploited as a detector material in a prototype fiber optic radiation sensor. The scintillation intensity from a [$Y_{1.9}O_3$; $Eu_{0.1}$, $Li_{0.16}$]-modified, 400 μm sized optical fiber tip, recorded using a CCD-photodetector and integrated over the 605–617 nm wavelength domain, was correlated with radiation exposure using a Precision XRAD 225Cx small-animal image guided radiation therapy (IGRT) system. At both 80 and 225 kVp energies, this radiotransparent device recorded scintillation intensities that tracked linearly with total radiation exposure in a micro-CT dual imaging and high precision cone-beam therapy instrument utilized for small-animal image guided radiation therapy (IGRT): these data highlight the capability of these nanomaterials to provide alternately accurate dosimetry measurements for both diagnostic imaging (80 kVp) and radiation therapy treatment (225 kVp), and underscore one potential role for [$Y_{2-x}O_3$; Eu_x, Li_y] nanoscale scintillating materials in medicine.

Supplementary Material

Refer to Web version on PubMed Central for supplementary material.

Acknowledgments

This study was supported in part by grants from the Department of Homeland Security, Domestic Nuclear Detection Office - Academic Research Initiative (NSF-ECCS-11-40037), the National Aeronautics and Space Administration (NNX11AC60G), the U.S. NRC Health Physics Fellowship (NRC-HQ-12-G-38-0022), and the National Institute of Allergy and Infectious Diseases (5U19AI067798).

Notes and references

1. Rodnyi, PA. Physical Processes in Inorganic Scintillators. CRC Press; 19997.
2. Nikl M. Meas Sci Technol. 2006; 17:R37–R54.
3. van Eijk CWE. Phys Med Biol. 2002; 47:R85–R106. [PubMed: 12030568]
4. Ozawa L, Itoh M. Chem Rev. 2003; 103:3835–3855. [PubMed: 14531714]
5. Duclos SJ, Greskovich CD, Lyons RJ, Vartuli JS, Hoffman DM, Riedner RJ, Lynch MJ. Nucl Instrum Methods Phys Res, Sect A. 2003; 505:68–71.
6. Dai Q, Foley ME, Breshike CJ, Lita A, Strouse GF. J Am Chem Soc. 2011; 133:15475–15486. [PubMed: 21863840]
7. Gupta BK, Narayanan TN, Vithayathil SA, Lee Y, Koshy S, Reddy ALM, Saha A, Shanker V, Singh VN, Kaipparettu BA, Marti AA, Ajayan PM. Small. 2012; 8:3028–3034. [PubMed: 22807340]
8. Wakefield G, Holland E, Dobson PJ, Hutchison JL. Adv Mater. 2001; 13:1557–1560.

9. Brown, SS.; Rondinone, AJ.; Dai, S. Antiterrorism and Homeland Defense: Polymers and Materials. Reynolds, JG.; Lawson, GE.; Koester, CJ., editors. 2007. p. 117
10. Letant SE, Wang TF. Nano Lett. 2006; 6:2877–2880. [PubMed: 17163723]
11. Sun C, Pratx G, Carpenter CM, Liu HG, Cheng Z, Gambhir SS, Xing L. Adv Mater. 2011; 23:H195–H199. [PubMed: 21557339]
12. Letant SE, Wang TF. Appl Phys Lett. 2006; 88:103110.
13. Dujardin C, Amans D, Belsky A, Chaput F, Ledoux G, Pillonnet A. IEEE Trans Nucl Sci. 2010; 57:1348–1354.
14. Stanton IN, Ayres JA, Therien MJ. Dalton Trans. 2012; 41:11576–11578. [PubMed: 22940914]
15. Ye T, Zhao GW, Zhang WP, Xia SD. Mater Res Bull. 19997; 32:501–506.
16. Repelin Y, Proust C, Husson E, Beny JM. J Solid State Chem. 19995; 118:163–169.
17. Yi SS, Shim KS, Yang HK, Moon BK, Choi BC, Jeong JH, Kim JH, Bae JS. Appl Phys A: Mater Sci Process. 2007; 87:667–671.
18. Bae JS, Yoon JH, Park SK, Kim JP, Jeong ED, Won MS, Jeong JH, Shim KS, Yang HK, Yi SS. Surf Rev Lett. 2007; 14:535–538.
19. Ray S, Pramanik P, Singha A, Roy A. J Appl Phys. 2005; 97:094312.
20. Tallant DR, Seager CH, Simpson RL. J Appl Phys. 2002; 91:4053–4064.
21. Buchanan RA, Wickersheim KA, Weaver JL, Anderson EE. J Appl Phys. 1968; 39:4342–4347.
22. Yeh SM, Su CS. Mater Sci Eng, B. 19996; 38:245–249.
23. Yi SS, Bae JS, Shim KS, Jeong JH, Park JC, Holloway PH. Appl Phys Lett. 2004; 84:353–355.
24. Abrams BL, Holloway PH. Chem Rev. 2004; 104:5783–5801. [PubMed: 15584688]
25. Berger, MJ.; Hubbell, JH.; Seltzer, SM.; Chang, J.; Coursey, JS.; Sukumar, R.; Zucker, DS.; Olsen, K. XCOM: Photon Cross Section Database (Version 1.5). National Institute of Standards and Technology; Gaithersburg, MD: 2010. http://physics.nist.gov/xcom
26. Attix, FH. Introduction to Radiological Physics and Radiation Dosimetry. John Wiley & Sons, Inc.; 1986.
27. Dawson LA, Jaffray DA. J Clin Oncol. 2007; 25:938–946. [PubMed: 17350942]
28. Klein D, Briere TM, Kudchadker R, Archambault L, Beaulieu L, Lee A, Beddar S. Radiat Meas. 2012; 47:921–929. [PubMed: 23180976]
29. Archambault L, Briere TM, Ponisch F, Beaulieu L, Kuban DA, Lee A, Beddar S. Int J Radiat Oncol, Biol, Phys. 2010; 78:280–287. [PubMed: 20231074]
30. Archambault L, Arsenault J, Gingras L, Beddar AS, Roy R, Beaulieu L. Med Phys. 2005; 32:2271–2278. [PubMed: 16121582]

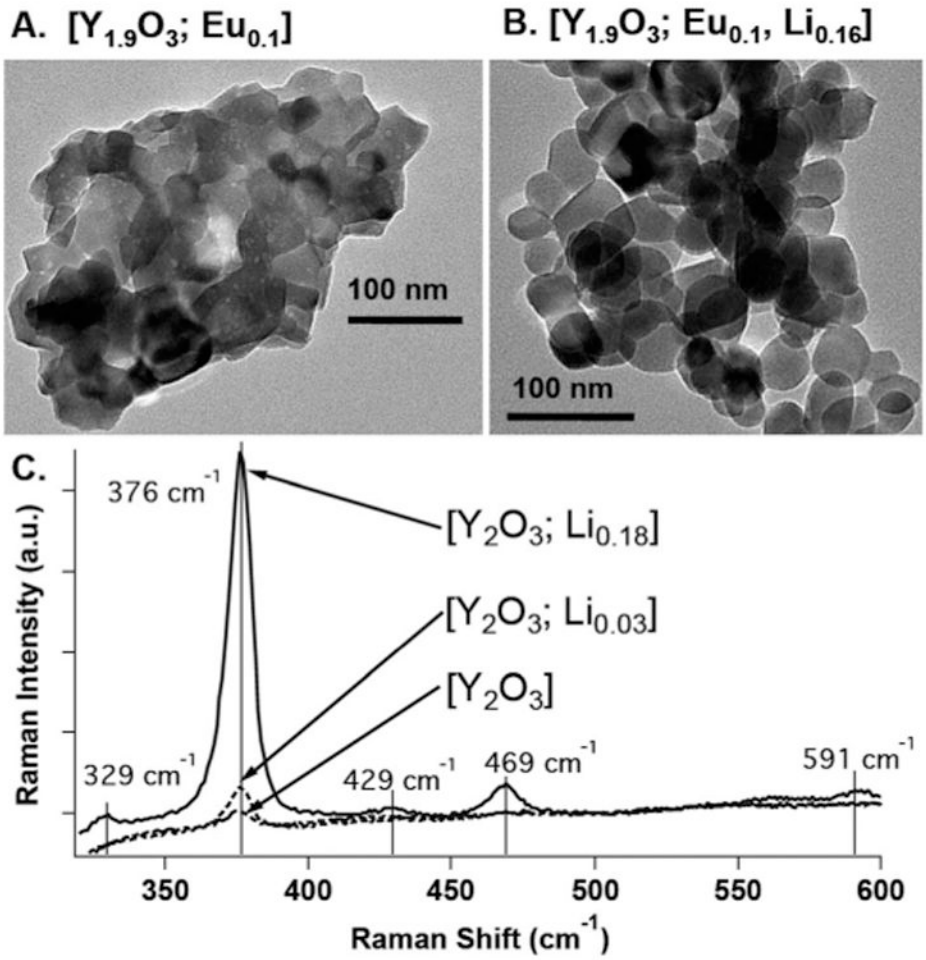

Fig. 1.

TEM images of: (A) [$Y_{1.9}O_3$; $Eu_{0.1}$] and (B) [$Y_{1.9}O_3$; Eu_0.1, $Li_{0.16}$] nanocrystal compositions. (C) Raman spectra of [Y_2O_3; Li_y] compositions acquired at a 632 nm irradiation wavelength. The increases in size and crystallinity observed in the TEM images as a function of increased Li concentration correlate with an observed increase in the Raman scattering intensity measured at 376 cm^{-1}.

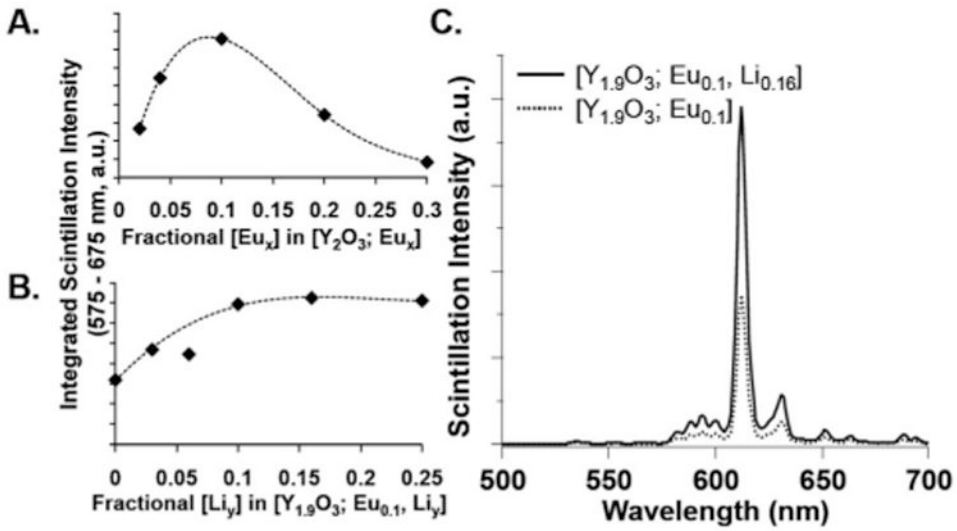

Fig. 2.

Integrated, solid-state X-ray emission spectral intensities determined over a 575–675 nm range for: (A) [Y_2O_3; Eu_x] and (B) [$Y_{1.9}O_3$; $Eu_{0.1}$, Li_y] compositions (note: trend lines added for visualization purposes). (C) The X-ray emission spectra of the most emissive Eu and Eu/Li co-doped samples, recorded for 130 kVp (5 mA) X-ray excitation.

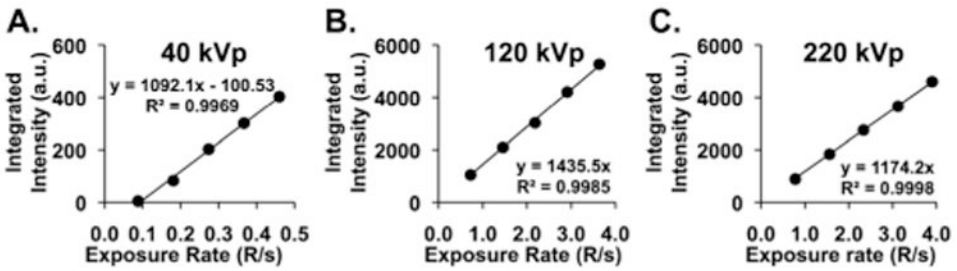

Fig. 3.

Integrated solid-state X-ray emission spectral intensity recorded over the 500–700 nm range as a function of radiation exposure (R s^{-1}) for: (A) 40, (B) 120, and (C) 220 kVp excitation.

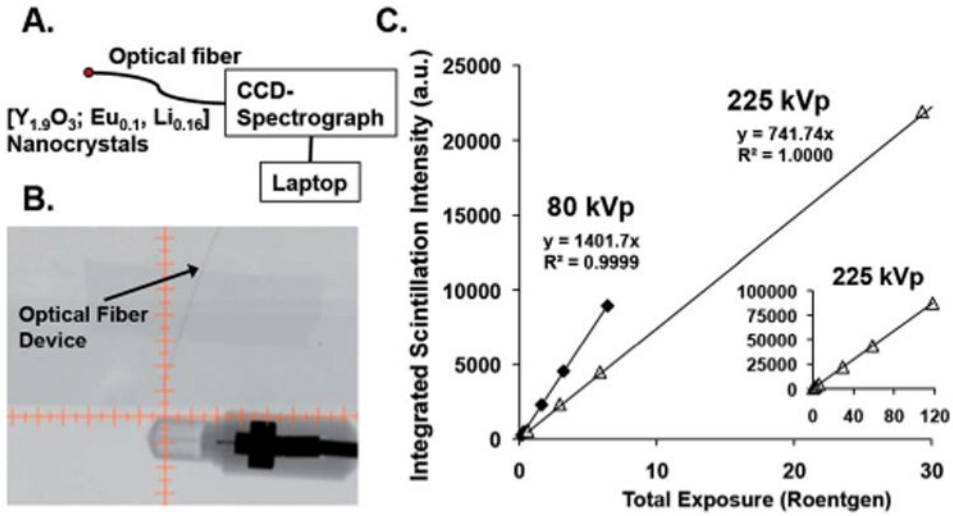

Fig. 4.

(A) A schematic of the sub-mm-sized optical fiber prototype dosimeter based on nanoscale [$Y_{1.9}O_3$; $Eu_{0.1}$, $Li_{0.16}$]. (B) An X-ray CT image acquired at 40 kVp, showing the optical fiber device adjacent to an ion-chamber radiation detector. (C) The linear scintillation intensity recorded by the device integrated over 605–617 nm that measures the total dose deposited at 80 kVp (imaging) and 225 kVp (therapy) energies. The CT image was acquired in a Precision XRAD 225Cx small-animal image guided radiation therapy (IGRT) system; the scintillation data were recorded using IGRT 80 and 225 KVp excitation. Note that all data points were measured in triplicate, and the standard deviation for a given data point was <0.9%. The inset of (C) shows that the device scintillation response tracks linearly with exposure to the highest levels tested (117.8 Roentgen at 225 kVp).